A vision-based blind spot warning system for daytime and nighttime driver assistance ☆

Bing-Fei Wu [a], Hao-Yu Huang [a], Chao-Jung Chen [b], Ying-Han Chen [a], Chia-Wei Chang [a], Yen-Lin Chen [c,*]

[a] Dept. of Electrical and Control Engineering, National Chiao Tung University, Hsinchu 30050, Taiwan
[b] CSSP Inc., Hsinchu, Taiwan
[c] Dept. of Computer Science and Information Engineering, National Taipei University of Technology, Taipei 10608, Taiwan

ARTICLE INFO

ABSTRACT

This paper proposes an effective blind spot warning system (BSWS) for daytime and nighttime conditions. The proposed BSWS includes camera models of a dynamic calibration and blind spot detection (BSD) algorithms for the daytime and nighttime. Under daytime conditions, the proposed system presents the Horizontal Edge and Shadow Composite Region (HESCR) method to extract the searching region and to acquire the shadow location of the targeted vehicles. Additionally, to detect vehicles at nighttime road scenes, the proposed system extracts bright objects and recognizes the paired headlights of the targeted vehicles for the BSD. The BSWS is implemented on a DSP-based embedded platform. The results of the BSWS are obtained by conducting practical experiments on our camera-assisted car on a highway in Taiwan under both nighttime and daytime conditions. Experimental results show that the proposed BSWS is feasible for vehicle detection and collision warning in various daytime and nighttime road environments.

© 2013 Elsevier Ltd. All rights reserved.

1. Introduction

Recently, driving safety has become one of the most critical concerns. Because car accidents frequently occur, intelligent vehicle technologies are rapidly advancing worldwide [1,2]. Previous studies have indicated that intelligent vehicle technologies enhance road transportation efficiency and increase driving pleasure. Within the research areas of intelligent transportation systems, driving assistance plays a vital role in protecting driver safety and prevents car collisions. Because human vision weakens while driving, scientists and scholars have focused on detecting obstacles in front of the host car. The aforementioned works promote driver safety using front and rear vision. However, collision accidents occurring in a vehicle's BSR is a more serious problem.

Therefore, this study presents a BSWS compatible with daytime and nighttime uses. The introduced architecture applies two algorithms focusing on the characteristics of daytime and nighttime conditions with low computational complexity and high precision accuracy. The proposed BSWS is a fully vision-based detection system using only two cameras, which are installed below the rear view mirror on both sides of our camera-assisted experimental car, a Taiwan iTS-II. By setting the CCD cameras below both sides of the rear view mirrors, the proposed system obtains road conditions and determines
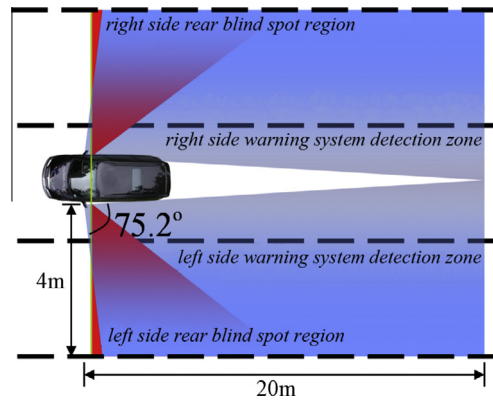

Fig. 1. Vertical view of the warning system detection zone.

whether there are any accidents occurring in the BSR. The vertical overview of the proposed system is shown in Fig. 1. The horizontal viewing angle between the cameras and the body of the car is 75.2°. The detection zone covers 20 m behind the camera and a 4-m width on both sides.

The images captured by cameras are analyzed using the proposed vision-based algorithms, such as edge detection methods [3–5], morphological image processing [6–10], and other computer vision techniques. First, the camera models are established using a dynamic calibration method, and the corresponding transform of the 2D image plane and 3D world coordinate are derived. After the camera calibration is completed, practical roadway information can be efficiently obtained. In the next step, this study presents an edge-based BSD approach for daytime conditions, and a paired-headlight-based BSD approach for nighttime conditions. Under daytime conditions, the shadow edge features of the vehicle object are extracted using minimum ground plane pre-processing and continuous level shadow detection techniques. The minimum ground plane is obtained using the HESCR, and the horizontal and continuous scanning is then performed on the minimum ground plane to specialize the shadow positions. Moreover, this study also presents a solution for eliminating false detections of non-vehicle obstacles. Under nighttime conditions, this study adopted a bright object segmentation method to extract bright objects that possibly indicate vehicle lamps under nighttime conditions. The extracted bright objects are analyzed to determine whether they are lamp objects. The potential vehicle lamp objects are then verified to determine whether two of the lamp objects can be paired. Vehicles in the nighttime are detected if the paired-headlights are found. Additionally, an efficient vehicle distance estimation method is also presented. Mastering the distance between the host car and approaching vehicles allows the system to forewarn the driver to avoid possible collisions.

With the growth of the embedded hardware, some previous works have implemented BSD systems using real-time embedded applications [12,13]. Thus, the proposed BSWS is implemented on a portable DSP-based embedded platform [11]. The experimental results are evaluated under both daytime and nighttime conditions. The proposed system was tested on our experimental car for more than 30 min to guarantee robustness, and the experimental results demonstrate that the proposed system can achieve a high detection accuracy of over 90% under both daytime and nighttime conditions. In addition, the proposed system is also compared with other relevant methods. The comparative and experimental results show that the proposed BSWS system can provide favorable performance in vehicle detection and collision warning, despite blind spots under both daytime and nighttime conditions.

The features and contributions of this study are as follows:

(1) The proposed BSWS is a fully vision-based BSD system by using computer vision techniques, such as dynamic camera calibration and image pre-processing methods. Therefore, the proposed BSWS can be easily implemented only using cameras as sensors.
(2) This study presents two vision-based BSD algorithms according to daytime and nighttime conditions. For daytime and nighttime conditions, this study presents an edge-based approach and a paired-headlight-based approach to detect the shadow regions and paired headlights of vehicle obstacles as features for BSD.
(3) Additionally, the proposed BSWS is implemented on a DSP-based platform for practical demonstration. This study evaluates the proposed system in practical by using only two cameras, which are installed below the rear view mirror on both sides of our camera-assisted experimental car, a Taiwan *i*TS-II. The experimental results of the proposed BSWS are evaluated under both daytime and nighttime conditions.

This paper is organized as follows. Section 2 presents a review of literature in the area of driving assistance and BSD. Section 3 presents an efficient camera model with a dynamic calibration model. Section 4 shows the proposed two algorithms of the BSWS for both daytime and nighttime, including the vehicle distance estimation method. The experimental

results are shown in Section 5. Finally, Section 6 offers the conclusions to this paper. Besides, this study uses several abbreviations for concise writing.

2. Related works

Numerous studies have proposed novel methods to solve this problem during the day [14,15] and night [16–18]. To improve the performance of detection obstacles in the front view, some studies attempt to increase sensors mounted on vehicles. Rodríguez Flórez et al. adopt two cameras for stereo vision, multi-layer RADAR and CAN-bus sensors to vehicles and pedestrians [14]. Jia et al. employee multi-range RADARs and several cameras to detect multi-model obstacles [15]. Under nighttime conditions, a paired-lamp-based detection method using bright object segmentation is employed to determine the vehicles appearing in front of the host car. Wang et al. presented a taillight extraction and paring method to detect front cars [16]. Fossati et al. proposes a real-time vehicle detecting and tracking system based on the HSV of taillight [17]. Furthermore, O'Malley et al. realized rear-lamp extraction and pairing and implemented lamp tracking using Kalman filters [18]. However, rear vision is also a critical concern. Recently, pattern recognition techniques [19] are widely developed and applied on intelligent vehicular technologies. Lin and Xu presented a vision-based method for detecting the vertical edges of vehicles behind the host car [20].

Although most attention was fascinated with the frontview obstacle and lane detection, some previous studies have attempted to solve the problem of blind spot detection (BSD) [21–29]. Wong and Qidwai installed six ultrasonic sensors and three cameras to obtain the surrounding information of the host car. The obtained data were then processed using fuzzy inference to forewarn the driver before the collision occurs [21]. Ruder et al. adopted RADAR and image sensors to acquire the speed and position of the vehicle in the BSR [22]. Both [21,22] built the system architecture by integrating both cameras and other detection sensors. Numerous other works have introduced a vision-based method to reduce cost. Otto et al. also adopted cameras and RADARs as BSD sensors, but this study focuses on detecting the pedestrians and keeping pedestrians safety while walking across roads [23]. Achler and Trivedi used an omni-directional camera to monitor the surroundings of the host car. The wheel data in the captured images are filtered by the 2D filter banks and are used to distinguish the vehicles in the BSR [24]. Techmer [25] utilized inverse perspective mapping and an edge extraction algorithm to match the pattern and to determine whether any vehicle exists in the BSR. Díaz et al. applied an optical flow algorithm to extract the vehicles in the BSR and to track the target vehicle using several scale templates and Kalman filters [26]. Although [24–26] have obtained the surrounding information of the host car using specialized sensors or processors, the computational costs of image preprocessing are substantial. Krips et al. introduced the adaptive template matching method, which is characterized according to the self-adjusted template to detect the vehicles approaching the host car in the BSR [27]. Jeong et al. presented a morphology-based saliency map model and combined it with Scale Invariant Feature Transform (SIFT) [30]. Lin et al. proposed a vision-based BSD by pattern recognition techniques. The edge features of vehicles are first trained as a detector, and the trained edge detector is used to recognize the vehicles in BSD, The related studies [27,28] have distinguished the vehicle according to an established database of the vehicle objects. The detecting method, using the feature and templates, can supply effective classification for common vehicles in the daytime, but this method may not perform effectively in the nighttime. Li et al. demonstrated the BSD by using fisheye cameras [29]. However, the scenario stated in [29] is for parking assistance, rather than on-road driving assistance applications.

3. Camera model with dynamic calibration

This section presents the camera projection model to transform the 2D image plane and the 3D world coordinate system. The proposed camera model also contains the parameter settings and the camera calibration process. In this section, the details of the proposed camera model, including the perspective transformation, transformation between the 2D image and the 3D world coordinates, and adjustment of the uneven pavement is illustrated.

The position of any point (X_c, Y_c, Z_c) in the camera projection on a 2D image plane (u, v) can be obtained using perspective transformation. Fig. 2a shows the model of image objects captured by the camera being projected onto the 2D image coordinates, where X_c and Z_c in this camera projection model correspond to u and v in the 2D image coordinate, respectively. In the following description, we introduce the transforms from the camera coordinate to the 2D image coordinate. In the proposed transforms, Y_c, which denotes the perception depth, is the key parameter.

Using the perspective transformation, it is observed that

$$\frac{udu}{f} = \frac{x}{y}, \quad \frac{vdv}{f} = \frac{z}{y} \tag{1}$$

Eq. (1) can be rewritten as

$$u = e_u \frac{X_c}{Y_c}, \quad v = e_v \frac{Z_c}{Y_c} \tag{2}$$

where e_u and e_v represent as $\frac{f}{du}$ and $\frac{f}{dv}$, respectively. x, y and z in Eq. (1) are substituted with X_c, Y_c and Z_c, respectively.
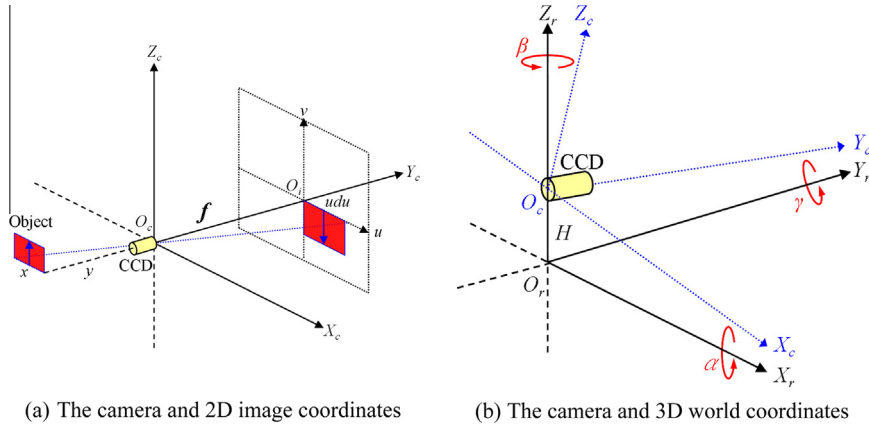
(a) The camera and 2D image coordinates   (b) The camera and 3D world coordinates

Fig. 2. Relationships between the camera, 2D image and 3D world coordinates.

Let $\mathbf{P}_{proj}$, $\vec{I}_h$ and $\vec{C}_h$ be a perspective transformation matrix, the vectors of the 2D image and camera coordinates, respectively. It can be observed that

$$\mathbf{P}_{proj} = \begin{bmatrix} e_u & 0 & 0 & 0 \\ 0 & 1 & 0 & 0 \\ 0 & 0 & e_v & 0 \\ 0 & 0 & 0 & 1 \end{bmatrix}, \quad \vec{I}_h = [x_i \quad y_i \quad z_i \quad 1]', \quad \vec{C}_h = [X_c \quad Y_c \quad Z_c \quad 1]' \tag{3}$$

By applying Eq. (3), the relationships between $\vec{I}_h$, $\vec{C}_h$, and $\mathbf{P}_{proj}$ can be formulated as Eq. (4) as follows:

$$\vec{I}_h = \mathbf{P}_{proj}\vec{C}_h \tag{4}$$

As Fig. 2b shows, (X_c, Y_c, Z_c) and (X_r, Y_r, Z_r) represent the camera and 3D world coordinates, respectively. By shifting and rotating (X_r, Y_r, Z_r), (X_c, Y_c, Z_c) is acquired. Let W_h be the vector of the 3D world coordinate. Thus, the relationship between C_h and W_h can be rewritten as

$$\vec{C}_h = \mathbf{R}_x(\vec{W}_h - \vec{T}) \tag{5}$$

where $\mathbf{R}_x$ and $\vec{T}$ denote the 4×4 rotating matrix the 4×1 shifting vector between $\vec{C}_h$ and $\vec{W}_h$, respectively. O_c and O_r represent the origins of the camera and 3D world coordinates. Let H be the distance between O_c and O_r. Then T can be represented as Eq. (6).

$$\vec{T} = [0 \quad 0 \quad H \quad 0]' \tag{6}$$

Here, as Eq. (7) shows, the rotating matrix $\mathbf{R}_x$ is decomposed to three matrices $\mathbf{R}_\alpha$, $\mathbf{R}_\beta$, and $\mathbf{R}_\gamma$. α, β, and γ denote the counterclockwise rotation angle within the X axis, Z axis, and Y axis, respectively. Additionally, α, β, and γ respectively represent the "tilt angle," "pan angle," and "swing angle" in the practical case examined in this study. Accordingly, $\mathbf{R}_\alpha$, $\mathbf{R}_\beta$, and $\mathbf{R}_\gamma$ are obtained using Eq. (8).

$$\mathbf{R}_x = \mathbf{R}_\alpha \mathbf{R}_\beta \mathbf{R}_\gamma \tag{7}$$

$$\mathbf{R}_\alpha = \begin{bmatrix} 1 & 0 & 0 & 0 \\ 0 & \cos\alpha & -\sin\alpha & 0 \\ 0 & \sin\alpha & \cos\alpha & 0 \\ 0 & 0 & 0 & 1 \end{bmatrix}, \quad \mathbf{R}_\beta = \begin{bmatrix} \cos\beta & -\sin\beta & 0 & 0 \\ \sin\beta & \cos\beta & 0 & 0 \\ 0 & 0 & 1 & 0 \\ 0 & 0 & 0 & 1 \end{bmatrix}, \quad \mathbf{R}_\gamma = \begin{bmatrix} \cos\gamma & 0 & -\sin\gamma & 0 \\ 0 & 1 & 0 & 0 \\ \sin\gamma & 0 & \cos\gamma & 0 \\ 0 & 0 & 0 & 1 \end{bmatrix} \tag{8}$$

The rotation angle within the Y axis does not exist in the case involving a blind spot. Therefore, the swing angle γ is zero, and then Eq. (7) is rewritten as Eq. (9).

$$\mathbf{R}_x = \mathbf{R}_\alpha \mathbf{R}_\beta = \begin{bmatrix} \cos\beta & -\sin\beta & 0 & 0 \\ \cos\alpha \cdot \sin\beta & \cos\alpha \cdot \cos\beta & -\sin\alpha & 0 \\ \sin\alpha \cdot \sin\beta & \sin\alpha \cdot \cos\beta & \cos\alpha & 0 \\ 0 & 0 & 0 & 1 \end{bmatrix} \tag{9}$$

Based on the results introduced in the previous two subsections, the perspective transformation between the 2D image and 3D world coordinates can be obtained. The relationship is shown as Eq. (10), which can be acquired using Eqs. (4) and (5).

$$\vec{I}_h = \begin{pmatrix} e_u \cdot (\cos \beta \cdot X_r - \sin \beta \cdot Y_r) \\ \cos \alpha \cdot \sin \beta \cdot X_r + \cos \alpha \cdot \cos \beta \cdot Y_r - \sin \alpha \cdot (Z_r - H) \\ e_v \cdot (\sin \alpha \cdot \sin \beta \cdot X_r + \sin \alpha \cdot \cos \beta \cdot Y_r + \cos \alpha \cdot (Z_r - H)) \end{pmatrix} \tag{10}$$

Additionally, the relationships of (u, v) and (X_r, Y_r, Z_r) are attained using Eqs. (2) and (10), respectively,

$$u = \frac{x_i}{y_i} = e_u \frac{\cos \beta \cdot X_r - \sin \beta \cdot Y_r}{\cos \alpha \cdot \sin \beta \cdot X_r + \cos \alpha \cdot \cos \beta \cdot Y_r - \sin \alpha \cdot (Z_r - H)} \tag{11}$$

$$v = \frac{z_i}{y_i} = e_v \frac{\sin \alpha \cdot \sin \beta \cdot X_r + \sin \alpha \cdot \cos \beta \cdot Y_r + \cos \alpha \cdot (Z_r - H)}{\cos \alpha \cdot \sin \beta \cdot X_r + \cos \alpha \cdot \cos \beta \cdot Y_r - \sin \alpha \cdot (Z_r - H)} \tag{12}$$

For the case of zero tilt angles, let $\alpha = 0$. Then Eqs. (11) and (12) can be rewritten as Eq. (13).

$$u = e_u \frac{\cos \beta \cdot X_r - \sin \beta \cdot Y_r}{\sin \beta \cdot X_r + \cos \beta \cdot Y_r}, \quad v = e_v \frac{Z_r - H}{\sin \beta \cdot X_r + \cos \beta \cdot Y_r} \tag{13}$$

In practical cases, the roads are usually non-flat. Thus, this subsection concerns the angle of inclination in real-life cases. Fig. 3 shows the angle of inclination θ. It is observed that

$$Z_r = \tan \theta \cdot Y_r = m_\theta \cdot Y_r \tag{14}$$

In Fig. 3, the road surface and the camera are parallel with an included edge angle θ. In this case, θ is equivalent to α, which is the tilt angle of the camera described in the previous subsection. Using Eqs. (13) and (14), the relationships of X_r, Y_r, and Z_r between the world coordinate system and the image coordinate system is declared in Eq. (15), respectively.

$$X_r = \frac{H\left(\sin \beta + \cos \beta \frac{u}{e_u}\right)}{m_\theta \left[\left(\cos \beta - \sin \beta \frac{u}{e_u}\right) - \frac{v}{e_v}\right]}, \quad Y_r = \frac{H\left(\cos \beta - \sin \beta \frac{u}{e_u}\right)}{m_\theta \left[\left(\cos \beta - \sin \beta \frac{u}{e_u}\right) - \frac{v}{e_v}\right]}, \quad Z_r = \frac{H\left(\cos \beta - \sin \beta \frac{u}{e_u}\right)}{\left(\cos \beta - \sin \beta \frac{u}{e_u}\right) - \frac{v}{e_v}} \tag{15}$$

The geometric lane model is approximated to a linear equation, as obtained using

$$X_r = m \cdot Y_r + b, \tag{16}$$

where m and b denote the slope and offset of the lane marking, respectively. There is an assumption that the coefficients in the 3D world coordinates are the same as those in the 2D image coordinates. Hence, the geometric lane model is transformed in the image domain, as obtained using

$$\frac{u}{e_u} = \left(\frac{-b}{(H \cos \beta + mH \sin \beta + bm_\theta \sin \beta)}\right) \cdot \frac{v}{e_v} + \left(\frac{(-H \sin \beta + mH \cos \beta + bm_\theta \cos \beta)}{(H \cos \beta + mH \sin \beta + bm_\theta \sin \beta)}\right) \tag{17}$$

Here, we can define,

$$M = \frac{-b}{H(\cos \beta + m \sin \beta) + bm_\theta \sin \beta}, \quad B = \frac{H(-\sin \beta + m \cos \beta) + bm_\theta \cos \beta}{H(\cos \beta + m \sin \beta) + bm_\theta \sin \beta} \tag{18}$$

$$U = \frac{u}{e_u}, \quad V = \frac{v}{e_v} \tag{19}$$

Then substituting Eqs. (18) and (19) into Eq. (17) can yields

$$U = MV + B, \tag{20}$$

Eq. (20) represents the lane model in terms of the image coordinates as well as the road inclination, m_θ, which is applied to the cases of non-flat roads.

Fig. 3. Angle of inclination between the vehicles and pavement.

4. Daytime and nighttime blind spot detection

This section presents the algorithm of BSD under daytime and nighttime conditions. Under daytime conditions, the regions of interest are determined according to the lane markings for detection efficiency and accuracy. After the ROI are determined, the edge of the shadow region is obtained using the proposed mechanisms, and the positions of the targeted vehicles in the BSR are detected according to the shadow edge. In addition, this section discusses how to eliminate non-vehicle obstacles, which are often misjudged as vehicle objects. Under nighttime conditions, the location of the paired head-lights is specified, and the vehicles in the BSR are located using the paired headlights.

4.1. ROI in daytime

The ROI detection under daytime conditions is based on information obtained using the lane marking detection process. The proposed ROI is initialized by detecting lane markings. The proposed system adopts a linear equation shown as Eq. (16) to approximate the model of lanes, which are calculated according to the Eq. (20). The detections of lane markings are performed by using the gray-level distribution of lane markings described in [32]. When the near-side marking line is detected in the captured images, modeling the marking lines with a linear equation is necessary. Fig. 4 illustrates the example of modeling the label lines in the 2D image and 3D real world coordinates. In Fig. 4a, it is obvious that two marking lines, which are the near side and the far side, are parallel in the 3D real world coordinates. Let the linear equations of the near-side and far-side label lines be $X_r = m_1 Y_r + b_1$ and $X_r = m_2 Y_r + b_2$, respectively. m_1 is equal to m_2 because the two label lines are parallel.

The corresponding relationship of the two label lines in the 2D image coordinate is shown in Fig. 4b. The linear equations of the detected near-side marking line in the 2D coordinate is $U = M_1 V + B_1$, which can be also obtained using the information of the captured images. The detection result of the near-side label line is shown as Fig. 5a. After the near-side marking line is acquired, the ROI is updated using the information of the detected marking line as shown in Fig. 4b. Because the near-side and far-side marking lines are parallel in the 3D world coordinate, let the line segment of the near-side $\overline{AD}$ be shifted 4 meters, and then $\overline{BC}$, which is the line segment of the far side, is obtained. Fig. 5b illustrates the corresponding image of $\overline{AD}$ and $\overline{BC}$ in the 2D image coordinate. The new ROI is enclosed using $\overline{AD}$, $\overline{BC}$, and the vanishing line. The range of the detected ROI is adjusted with the vanishing line adaptively. For example, using the camera with a 3.6 mm focal length, the maximum range of the detected ROI is approximately 20 m. The determination of *ABCD* consults the definition of lane change decision aid systems in ISO document [31]. According to the models described in [31], *ABCD* covers the left and right adjacent zones.

4.2. Image pre-processing

The captured blind spot images comprise two main parts, which are the ground plane and the obstacles. The main purpose of the blind spot detection is to detect whether the oncoming obstacles are vehicles. Therefore, eliminating the ground plane in the captured images is necessary. This subsection introduces the minimum ground method [33] to analyze the captured images and obtain the minimum ground plane. In addition, the salient features of the vehicles under daytime conditions are the shadows underneath the target vehicles. This study adopted the edge features of the shadows to extract the vehicle features in the captured images, as discussed in this subsection.

Before presenting the minimum ground statistic method, three assumptions should be addressed:

- The ground plane and obstacles make contact with each other.
- The boundaries between the ground plane and the obstacles are visible in the captured images.
- A boundary line exists, which is nearly horizontal between the ground plane and the obstacles in the captured images.
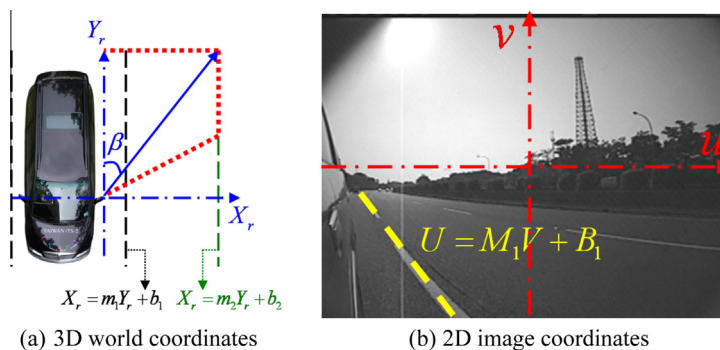

(a) 3D world coordinates   (b) 2D image coordinates

Fig. 4. Modeling the label lines in the 2D image and 3D real world coordinates.

(a) Result of the detection of the near-side label line
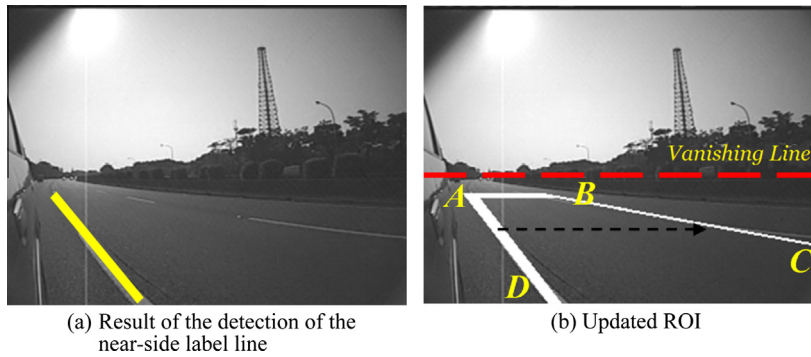
(b) Updated ROI

Fig. 5. Detection results of the near-lane marking line and updated ROI.

(a) Original image

(b) After performing the HESCR
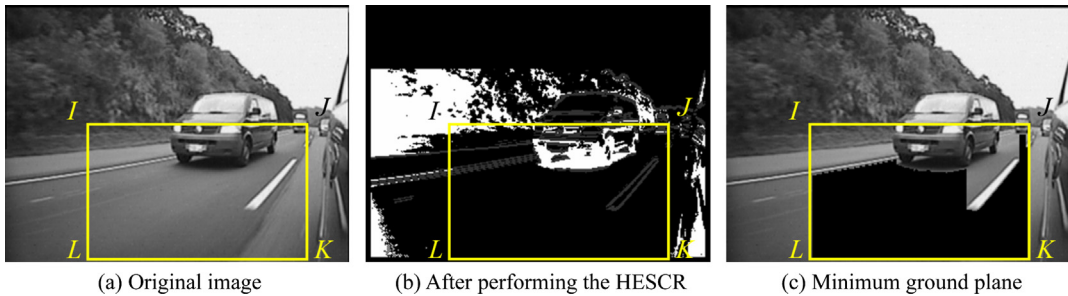
(c) Minimum ground plane

Fig. 6. Example of the minimum ground plane pre-processing.

Fig. 6 illustrates the minimum ground plane pre-processing. In Fig. 6a, the target of the process is to obtain the minimum ground plane *IJKL*. Thus, the proposed process uses the adopted horizontal Sobel edge extraction and obtains the HESCR, as shown in Fig. 6b. In Fig. 6b, the white and black regions denote the shaded regions and the ground regions, respectively, and the gray regions reflecting the boundaries between the white and black regions represent the horizontal edge area. After the horizontal Sobel edge extraction, the process begins scanning from the bottom-left to the top-right. The scanning process stops while the gray level of the scanned pixels are nonzero, which are the ground regions, and the remained black region is the minimum ground plane, as shown in Fig. 6c.

After the minimum ground plane is obtained, the average $\overline{G}_{MG}$ and the standard deviation σ_{MG} of the gray level of the pixels in the ground plane can be computed as Eq. (21). In Eq. (21), N and I_m denote the number of pixels and the gray level of the mth pixel in the minimum ground plane, respectively.

$$\overline{G}_{MG} = \frac{1}{N}\sum_{m=1}^{N} I_m, \quad \sigma_{MG} = \sqrt{\frac{1}{N}\sum_{m=1}^{N}(I_m - \overline{G}_{MG})^2} \tag{21}$$

(a) Sobel horizontal edge detector
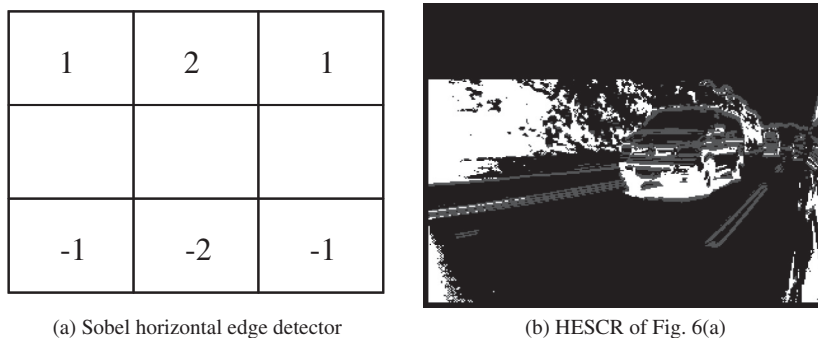
(b) HESCR of Fig. 6(a)

Fig. 7. Processing of HESCR.

The calculated $\overline{G}_{MG}$ and σ_{MG} are used to determine the threshold of distinguishing the ground plane and the vehicle objects adaptively. Thus, the effects caused by the different weather conditions and different sensitivity of the camera can be overcome.

The following description discusses how to calculate the HESCR, as shown in Fig. 7. Fig. 7a shows the Sobel horizontal edge detector which are used to filter the original image, such as that in Fig. 7a. The threshold of the Sobel binary plane is set to $\overline{G}_{MG}$ to eliminate the noise in the image. It is assumed that the gray levels of the shadow regions are lower than $\overline{G}_{MG}$, and the gray levels of the shadow regions are much lower than those of the other possible shadow regions. Thus, the threshold of the "dark" shadow regions is defined as $\overline{G}_{MG} - 2\sigma_{MG}$. The HESCR can be calculated using Eq. (22), where $df(u,v)/dv$ represents the gradient of the image in the v direction. Fig. 7b illustrates the calculated HESCR of Fig. 6a.

$$f_{\text{HESCR}}(u,v) = \begin{cases} 50, \text{if } df(u,v)/dv > \overline{G}_{MG} \\ 255, \text{if } df(u,v)/dv < \overline{G}_{MG} - 2\sigma_{MG} \\ 0, \text{otherwise} \end{cases} \tag{22}$$

4.3. Continuous level shadow detection

Under daytime conditions, the shadow of the bottom of the vehicles is also the main feature when recognizing the junction between the vehicle and the ground plane in the captured images. Fig. 8 illustrates the process of the continuous level shadow detection. In Fig. 8a, the continuous level scanning in the image is performed by applying Sobel edge extraction. The scanning horizontal levels begin from the bottom to the top of the images, and cross to the near-side and far-side marking lines at points F_P and N_P. Then, M_1, M_2, M_3, and M_4 are calculated using Eq. (23).

When the level scanning line moves upward, M_1, M_2, M_3, and M_4 meet the shadow region of the vehicle appearing in the ROI. When the gray levels of M_1, M_2, M_3, and M_4 are 255, the current level scanning line is the lower bound of the shadow region of the vehicle, and the interval width of F_P and N_P at this time is defined as the width of the region of the vehicle, which is denied as L_{RD}. In Fig. 8b, the shadow of the vehicle is projected on the width of the region of the vehicle. Although some of the projected lines of the shadow regions are shattered, most of them are close enough to be considered as connected lines. In the proposed algorithm, when the distances of a pair shattered lines is lower than $1/16L_{RD}$, these two shattered lines are connected. After the close shattered lines are connected, a maximum continuous projection line L_{VS} is observed. When L_{VS} is larger than a quarter of L_{RD}, it means that the detected shadow region is large enough, and the junction between the vehicle and the ground plane is detected in the ROI.

$$M_1 = \frac{1}{2}(F_P + M_2), \quad M_2 = \frac{1}{2}(F_P + N_P), \quad M_3 = \frac{1}{2}(M_1 + N_P), \quad M_4 = \frac{1}{2}(M_3 + N_P) \tag{23}$$

4.4. Non-vehicle obstacles elimination

It is observed that using the proposed shadow features to recognize the vehicles is efficient under daytime conditions. The bright objects, such as the zebra crossings and road markings shown in Fig. 9a and b, can be eliminated easily using the proposed algorithm. However, two frequently occurring conditions that are caused by the complicated shadows are described as follows. Fig. 25a and b illustrate examples of the long shadow region of vehicles and shadows of non-vehicle obstacles, respectively.

Most of the boundary features between the vehicle and the ground plane in the daytime can be detected using the proposed method in Section 4.2. But when vehicles drive in the dawn and nightfall times, the shadows lengthen because of the uprising and falling sunshine, respectively. As Fig. 10a shows, $\overline{CD}$ is the first detected shadow region, but it is not the suitable boundary between the vehicle and the ground plane. However, the shadow regions of the bottom of vehicles are darker than
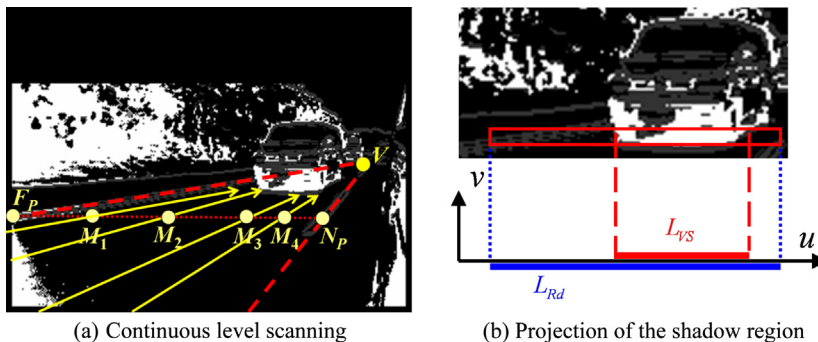

(a) Continuous level scanning   (b) Projection of the shadow region

Fig. 8. Process of the continuous level shadow detection.

(a) Example of bright   (b) Example of bright   (a) Example of the long   (b) Example of the shadows
objects: zebra crossings   objects: road markings   shadow region of vehicles   of non-vehicle obstacles
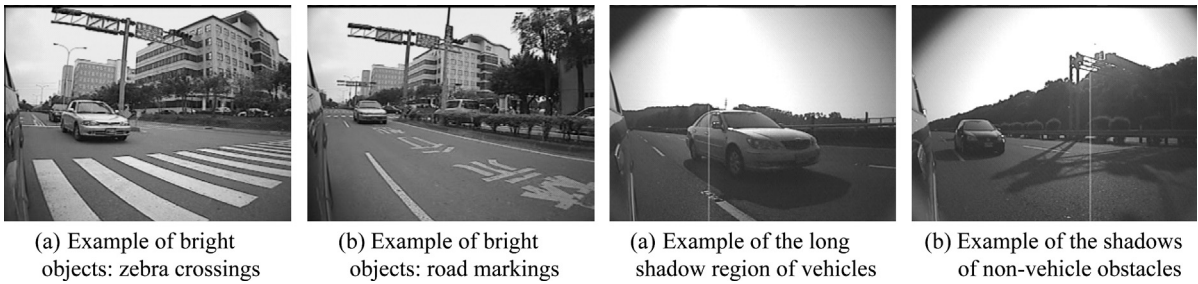
Fig. 9. Examples of bright objects and shadow regions.

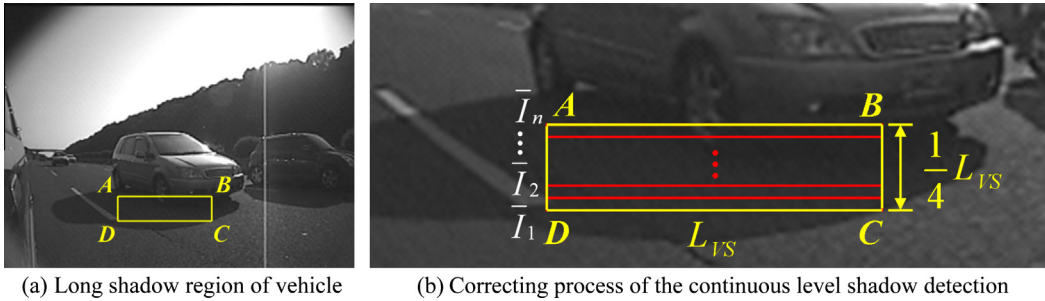(a) Long shadow region of vehicle   (b) Correcting process of the continuous level shadow detection

Fig. 10. Correction process based on the gray levels of the shadow regions.

those projected by the sunshine. To detect the shadow boundaries accurately, we present a correction process based on the gray levels of the shadow regions to contend with such a condition. According to the results of the continuous level shadow detection, $\overline{CD}$ corresponds to the maximum continuous projection line L_{VS}. The searching rectangular region $ABCD$ of the correction process is chosen, where the width and height of $ABCD$ are L_{VS} and $1/4L_{VS}$, respectively. As Fig. 10b shows, the searching order is from the bottom to the top of $ABCD$. Assume that $\overline{I}_n$ is the average gray level of the nth scanning line in $ABCD$. The boundary between the vehicle and the ground plane is calculated using Eq. (24).

$$v_{VS} = \arg \min_{j=1\sim n}(\overline{I}_j) \tag{24}$$

Another frequently occurring condition is when the shadow regions of non-vehicle obstacles have similar characteristics with those of actual vehicles. Fig. 11a indicates that $PQRS$ and $ABCD$ are detected using the proposed continuous level shadow detection method; but only $PQRS$ is the shadow region of the vehicle, whereas $ABCD$ is not. However, Fig. 11b shows that the vertical edges planes of $PQRS$ and $ABCD$ are distinguished. This study proposes a correction process for overcoming the non-vehicle obstacles.

To distinguish actual vehicle objects and non-vehicle obstacles accurately, the proposed architecture includes the correction process for eliminating non-vehicle obstacles. First, the correction process for the long shadow regions is employed to obtain the precise positions of junctions, such as $\overline{SR}$ and $\overline{CD}$ with length L_{VS} in Fig. 11c and d. The settings of searching regions are similar to those of the detection of long shadow regions. The searching regions $PQRS$ and $ABCD$ are chosen with the width L_{VS} and the height L_{VH}, which is set as $1/4L_{VS}$. After the searching regions are established, the captured image is transformed into the vertical edges planes, and $PQRS$ and $ABCD$ are enlarged to be analyzed, as shown in Fig. 11c and d, respectively. In the enlarged regions $PQRS$ and $ABCD$, the scanning vertical line orders from left to right, and u_{VB}^n represents the u coordinate of

(a) Error detection of the   (b) Vertical edge plane of (a)   (c) Enlarging $PQRS$ in (b)   (d) Enlarging $ABCD$ in (b)
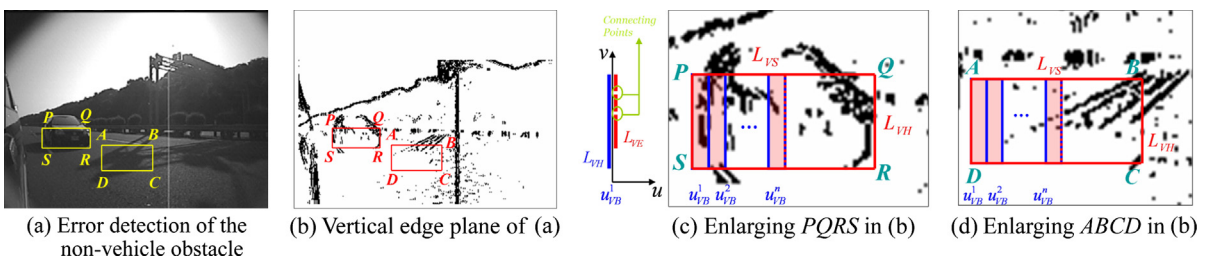non-vehicle obstacle

Fig. 11. Distinguishing actual vehicle objects and non-vehicle obstacles by the vertical edge plane.
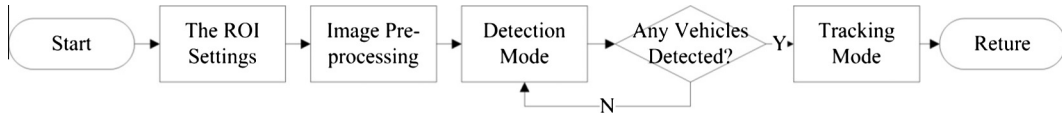
Fig. 12. Flow chart of the nighttime BSD.

the corresponding scanning vertical line, where n denotes the order of u_{VB} and begins from 1. The method exploited in Section 4.3 is then employed to obtain the maximum continuous projection line of the vertical edge L_{VE}, and u_{VB} is determined using Eq. (25). When there is no u_{VB} identified as 1, the searching region is determined as the non-vehicle object which edges are shattered. Otherwise, the searching region is determined as the vehicle object whereas at least one u_{VB} is detected as 1. The u coordinate of the detected vehicle object is then set as u_{VB}^m, whereas m is the smallest of n which corresponding u_{VB}^n is 1. Thus, the position of the vehicle object can be specified, and the non-vehicle object can be eliminated.

$$u_{VB}^n = \begin{cases} 1, & if\ L_{VE} > \frac{1}{2}\ L_{VH} \\ 0, & otherwise \end{cases} \tag{25}$$

4.5. Nighttime blind spot detection

The proposed nighttime BSD identifies vehicles by detecting and locating vehicle headlights using image segmentation and pattern analysis techniques. The flow chart of the proposed detection algorithm for nighttime conditions is shown in Fig. 12.

The ROI settings in the nighttime BSD are similar to those under daytime conditions. The upper bound of the ROI depends on the vanishing line of the image. However, the chosen ROI under nighttime conditions is fixed and not necessary to be updated. The image pre-processing procedure contains the bright objects segmentation and connecting components method [34]. After the image pre-processing, the bright objects are extracted and labeled. The labeled bright components would be recognized if they are the possible headlight objects.

In the detection mode of the nighttime BSD flow, the extracted and labeled bright objects are classified when the bright objects are the possible single headlight. The single headlight classification rules are shown as Eq. (26). A_{SL}^n and R_{SL}^n denote the area and the aspect ratio of the nth labeled bright component, respectively. $TH_{SLA_{UB}}$, $TH_{SLA_{LB}}$, $TH_{SLR_{UB}}$, and $TH_{SLR_{LB}}$ represent the upper and lower thresholds of the area and the aspect ratio of the single headlight, respectively. The standard deviation σ_{SL}^n of the gray levels of the nth labeled bright component is also adopted to distinguish when the bright components are the single headlight objects, and the upper bound threshold of σ_{SL}^n is $TH_{SL\sigma}$. According to the three rules listed in Eq. (26), the results of recognizing the nth labeled bright component, SL^n, are obtained. The bright component would be identified as the single headlight if SL^n is equal to 1. Otherwise, the bright component would not be classified as the single headlight and eliminated. These identified single headlight objects are merged and confirmed when they are paired headlight components.

$$SL^n = \begin{cases} 1, & if\ TH_{SLA_{LB}} < A_{SL}^n < TH_{SLA_{UB}}, \\ & TH_{SLR_{LB}} < R_{SL}^n < TH_{SLR_{UB}}, \\ & \sigma_{SL}^n < TH_{SL\sigma} \\ 0, & otherwise \end{cases} \tag{26}$$

The values of the thresholds in Eq. (26) are defined as follows. The threshold $TH_{SLR_{UB}}$ and $TH_{SLR_{LB}}$, are set as 1.2 and 0.8, respectively, to determine the circular-shaped appearance of a potential vehicle light. The threshold $TH_{SLA_{UB}}$ and $TH_{SLA_{LB}}$ are determined as $TH_{SLR_{UB}} = (LW(C_i)/4)^2$, and $TH_{SLR_{LB}} = (LW(C_i)/8)^2$, respectively, to adaptively reflect the reasonable area characteristics of a potential vehicle light. $LW(C_i)$ is the approximate lane width which is referred by [34], The threshold $TH_{SL\sigma}$ is set as 50 to ensure the reasonable luminance distribution of a potential vehicle light.

Eq. (27) shows the rules to determine whether the identified single headlight objects are merged as the paired headlight components. A_{ML}^n and R_{ML}^n denote the area and the aspect ratio of the nth merged single headlight objects, respectively. The area and aspect ratio of a pair of headlight components of a potential vehicle should follow the rule shown in Eq. (27), where $TH_{MLA_{UB}}$ and $TH_{MLA_{LB}}$ denote the upper and lower threshold of the area of the paired headlight component, respectively. Additionally, because the blind spot cameras are set precisely at the same height from the ground, the paired headlights of a vehicle in the BSR must locate objects at the same level. In other words, the vertical coordinates of the paired headlights should be almost the same. In the practical case, if the vertical coordinates of the merged single headlights are adequately close, the merged single headlights would be considered as the possible paired headlights, as shown in Eq. (27). $v_{SL^{nL}}$ and $v_{SL^{nR}}$ denote the left and right lamps of the merged single headlights, and TH_{VertD} is the threshold to assess whether these two lamps are close enough. Finally, the gray-level distribution of the paired headlight component is "light–dark–light." As Fig. 13 shows, the gray levels of pixels of the left and right headlights are much higher (lighter) than other regions. The gray levels of pixels in the region, which is between the paired headlights, are much lower (darker) than the lamp region. Therefore, the average luminance of the paired headlights $\overline{G}_{SL}^{nL}$ and $\overline{G}_{SL}^{nR}$ must be higher than that of the region between the paired headlights. The
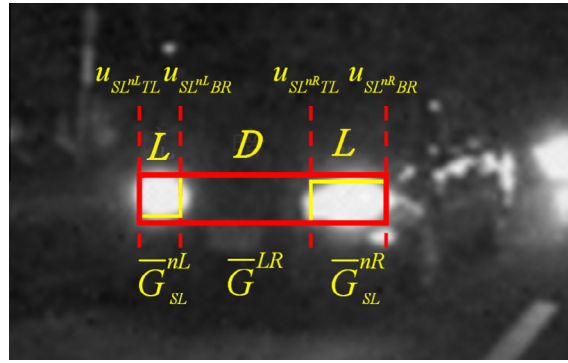
Fig. 13. Characteristic of the paired headlight component.

result A_{ML}^n is gained after checking the merged single headlights using Eq. (27). The merged single headlight would be determined as the pairing headlight component when ML^n is equal to 1.

$$ML^n = \begin{cases} 1, & if\ TH_{MLA_{LB}} < A_{ML}^n < TH_{MLA_{UB}}, R_{ML}^n < 1, \\ & |v_{SL^{nL}} - v_{SL^{nR}}| < TH_{VertD}, and \\ & \overline{G}_{SL}^{nL} > \overline{G}^{LR}, \overline{G}_{SL}^{nR} > \overline{G}^{LR} \\ 0, otherwise \end{cases} \tag{27}$$

The values of the thresholds in Eq. (27) are defined as follows. The threshold $TH_{MLA_{UB}}$ and $TH_{MLA_{LB}}$, are determined as $TH_{MLA_{UB}} = LW(G_i)$, and $TH_{MLA_{LB}} = 0.5 \cdot LW(G_i)$, respectively, to reveal the width property of the most types of different sized cars, such as sedans, buses, and trucks, appearing in the BSD. $LW(G_i)$ is the approximated lane width which is referred by [34].

In the tracking mode, this study consults the tracking process of vehicle component groups described in [34]. After the pairing headlight component is determined, the current coordinate of the pairing headlight component is recorded. The current coordinate of the detected paired headlight component is recorded. Since the vehicles are moving according to traffic flow, the coordinates are recorded five times and tested if the direction of recorded coordinates is the same as traffic flow. If so, the moving paired headlight component is recognized as the vehicle in the BSR.

4.6. Vehicle distance estimation

This subsection presents a geometric model of the lane departure based on the blind spot image and the vehicle distance estimation. Fig. 14a illustrates the relative positions of the blind spot camera and the lanes in the 3D real world, where the distance between the host vehicle and the right-side lane w_{dR} is composed of three parts, as shown in Eq. (28).

$$w_{dR} = w_1 + w_2 + w_v \tag{28}$$

where w_v, w_1 and w_2 represent half of the width of the host vehicle, the length of the blind spot camera, and the distance between the blind spot camera and the near-side label line in the pavement, respectively. Generally, w_v is fixed because of the standard specification of the vehicle, and w_1 is given because it depends on the specification of the camera. Therefore, to derive w_{dR}, calculating the value of w_2 is necessary.

Fig. 14b is the projection of 2D image coordinates to the 3D real world coordinates, and Fig. 14c is the detail of the geometric model. Let the blind spot camera and the host vehicle form an included angle β. From the viewpoint of the 2D image, the point O is the center point of the bottom of the captured images. To analyze the geometric model, three extended lines are drawn, as shown in Fig. 14c. First, draw an extended line from the bottom of the host vehicle and orthogonal to the driving direction of the host vehicle. Then draw another extended line from the blind spot camera to intersect with the previous extended line at the point O. The distance between the camera and O is Y_{hm}, and X_{lm} is orthogonal to Y_{hm} at O. Eq. (29) shows how to derive w_2 based on the model described in Fig. 14c.

$$w_2 = Y_{hm} \sin \beta - X_{lm} \cos \beta \tag{29}$$

The values of X_{lm} and Y_{hm} can be acquired using the information in the 2D image coordinates. X_{lm} is the distance from the point Y_{hm} to the closest lane in captured images. Let (u_{lm}, v_{lm}) be the 2D image coordinate of Y_{hm}. Furthermore, Y_{hm} is the distance from the point Y_{hm} to the blind spot camera. As Eq. (30) shows, X_{lm} and Y_{hm} can be calculated according to the camera models presented in Section 3.
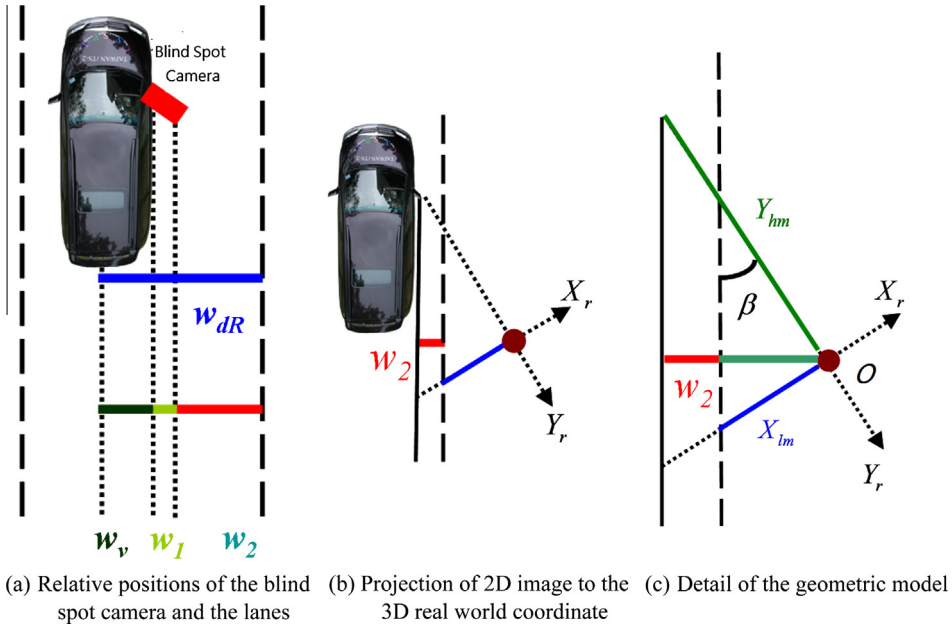
(a) Relative positions of the blind   (b) Projection of 2D image to the   (c) Detail of the geometric model
spot camera and the lanes   3D real world coordinate

Fig. 14. Geometric model of calculating w_{dR}.

$$X_{lm} = \frac{H\left(\sin\beta + \cos\beta\frac{u_{lm}}{e_u}\right)}{m_\theta\left(\cos\beta - \sin\beta\frac{u_{lm}}{e_u}\right) - \frac{v_{lm}}{e_v}}, \quad Y_{hm} = \frac{H\cos\beta}{m_\theta\cos\beta - \frac{v_{hm}}{e_v}} \tag{30}$$

Therefore, as Fig. 14c shows, w_2 can be obtained by substituting Y_{hm} and X_{lm}, and the distance between the vehicle and the right-side lane w_{dR} is also derived.

Fig. 15a illustrates the model of the vehicle distance estimation in the 3D world coordinate, where Y_{hv} is the distance from the blind spot camera to the target vehicle, D_{hl} is the distance between the vehicle and the near-side lane, D_{lv} is the distance between the target vehicle and the near-side lane, and D_{hv} is the vertical component of Y_{hv}. The vehicle distance estimation in the 2D image coordinate is shown in Fig. 15b, where Vk is the position underneath the host vehicle with the coordinate (u_{VCP}, v_{VCP}). Then draw a horizontal line through V. The horizontal line is also the junction between the vehicle and the ground plane and crosses the near-side lane with the point L with the coordinate (u_{NL}, v_{NL}). Thus, $v_{VCP} = -v_{NL}$, and Y_{hv} is obtained using Eq. (31), which is obtained using Eq. (15). Besides, to calculate the value of D_{lv}, it is necessary to obtain $\overline{LV}$, which is denoted as X_{lv}, in Fig. 15c at first. X_{lv} is employed using Eq. (31), which can be obtained using Eq. (15). The transform equation of D_{lv} and X_{lv} is described as Eq. (32). Finally, D_{lv} is derived using the Pythagorean Theorem described as Eq. (32).
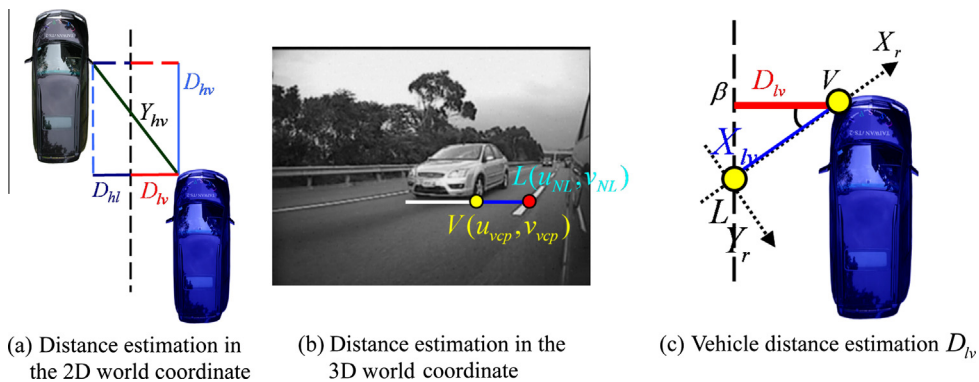

(a) Distance estimation in   (b) Distance estimation in the   (c) Vehicle distance estimation D_{lv}
the 2D world coordinate   3D world coordinate

Fig. 15. Vehicle distance estimation.

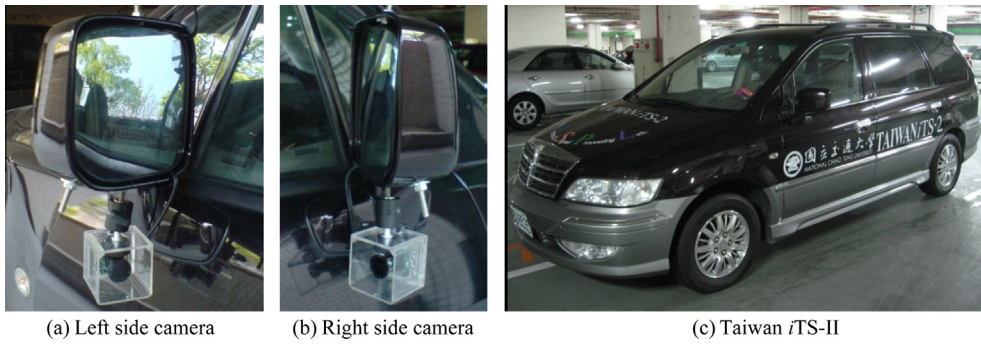(a) Left side camera   (b) Right side camera   (c) Taiwan *i*TS-II

Fig. 16. The proposed BSWS installed on our experimental car, the Taiwan *i*TS-II.

$$Y_{hv} = \frac{H\left(\cos\beta - \sin\beta\frac{u_{vcp}}{e_u}\right)}{m_\theta\left(\cos\beta - \sin\beta\frac{u_{vcp}}{e_u}\right) - \frac{v_{vcp}}{e_v}}, \quad X_{lv} = \frac{H\left(\sin\beta + \cos\beta\frac{\Delta u_{LV}}{e_u}\right)}{m_\theta\left(\cos\beta - \sin\beta\frac{\Delta u_{LV}}{e_u}\right) - \frac{v_{vcp}}{e_v}} \tag{31}$$

$$D_{lv} = X_{lv}\cos\beta, D_{hv} = \sqrt{Y_{hv}^2 - (D_{hl} + D_{lv})^2} \tag{32}$$

5. Experimental results

This section describes the implementation of the proposed blind spot detection and warning system. This study conducted various real on-road experiments on our experimental car to evaluate the vehicle detection performance, and perform comparative evaluations with the existent techniques to demonstrate the advantages of the proposed system.

5.1. Experimental environments

The proposed system was tested on several videos of real nighttime highway scenes under daytime and nighttime conditions in Taiwan. The proposed BSD system was implemented on a TI DM642 DSP-based embedded platform, operating at 600 MHz with 32 MB DRAM.

Fig. 16 illustrates that the BSD system was installed on our experimental car, the Taiwan *i*TS-II, with micro cameras. The established cameras are used to capture the images in the blind spot regions (BSRs), and then the proposed system on DM642 analyze the captured images and provide the real-time information for the driving assistance. The warning module alarms the drivers when the system detects the vehicles coming close in the BSR. The operation architecture is shown in Fig. 17. The proposed BSD system takes an average of 20 and 50 frames per second on daytime and nighttime. For the quantitative evaluation of vehicle detection performance, this study adopts the Jaccard coefficient [35], which is commonly used for evaluating performance in information retrieval. This measure is defined as,
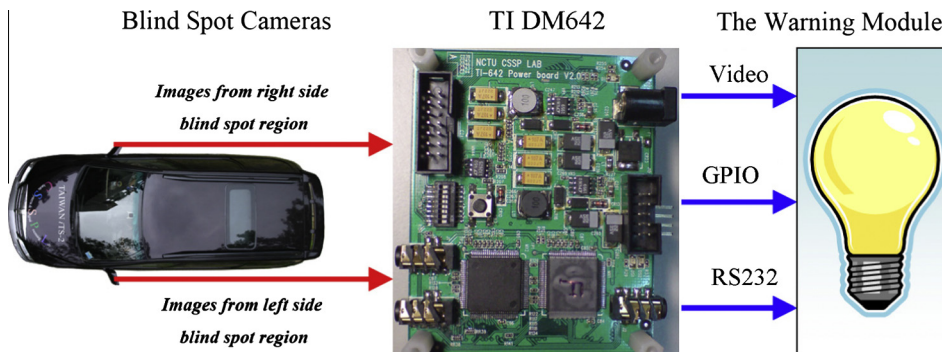
$$J = \frac{T_p}{T_p + F_p + F_n} \tag{33}$$

Fig. 17. The proposed BSWS implementation on DSP.

where T_p (true positives) represents the number of correctly detected vehicles, F_p (false positives) represents the number of falsely detected vehicles, and F_n (false negatives) is the number of missed vehicles. We determined the Jaccard coefficient J for the vehicle detection results of each frame of the traffic video sequences by manually counting the number of correctly detected vehicles, falsely detected vehicles, and missed detections of vehicles in each frame. The average value of the Jaccard coefficients J was then obtained from all frames of the video sequences using

$$\bar{J} = \sum_N J/N \tag{34}$$

where N is the total number of video frames. Here, the ground-truth of detected vehicles was obtained by manual counting.

5.2. On-road evaluation and performance comparisons

This subsection presents the on-road experimental results of the proposed BSWS. Figs. 18 and 19 and Tables 1 and 2 exhibit the most representative experimental samples of traffic scenes under different weather conditions regarding physical performance evaluation. First, Fig. 18 is a daytime highway traffic scene, where the detection results and the demonstration of the warning system are illustrated. Where a vehicle is detected in the blind spot region (BSR), the front of the detected vehicle is illustrated with a rectangle; and the distance between the driving and targeted vehicles is estimated, as Fig. 18a shows. When the detected vehicle approaches the driving vehicle and enters the warning zone, the proposed system alerts the drivers with the blinking rectangular sign, as Fig. 18b shows. However, some detection errors may occur when cars pass through the viaduct. Table 1 depicts the quantitative results of the proposed approach for vehicle blind spot detection
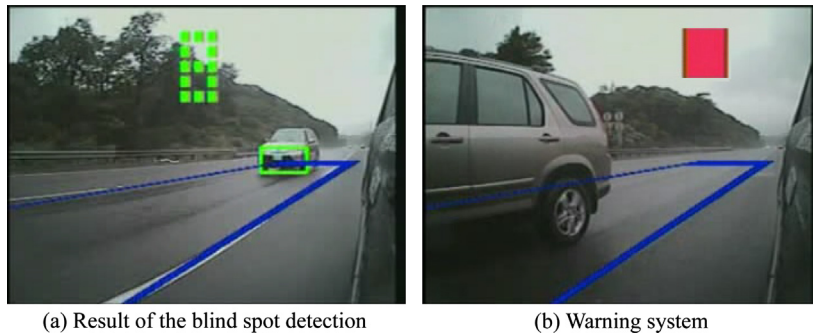

(a) Result of the blind spot detection   (b) Warning system

Fig. 18. Results of the blind spot detection and the warning system under daytime conditions.

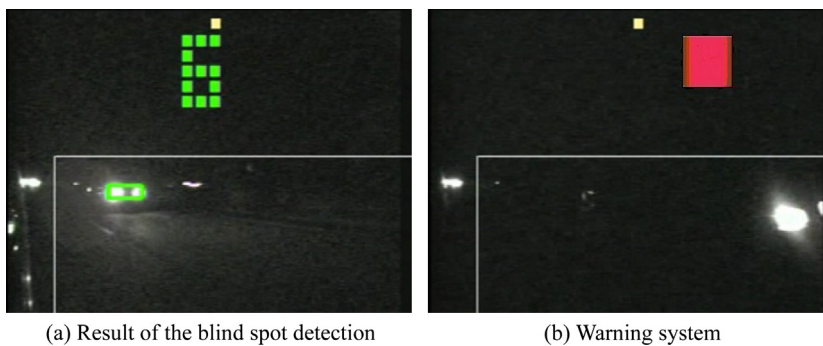(a) Result of the blind spot detection   (b) Warning system

Fig. 19. Results of the blind spot detection and warning system under nighttime conditions.

Table 1
Experimental data of the proposed system under daytime conditions, as shown in Fig. 18.

Lane	Detected vehicles	Falsely detected vehicles	Actual vehicles
Total no. vehicles in BSR	70	0	72
Detection score J of vehicles	97.22%		
Time span of the video	36 min		

Table 2

Experimental data of the proposed system under daytime conditions, as shown in Fig. 19.

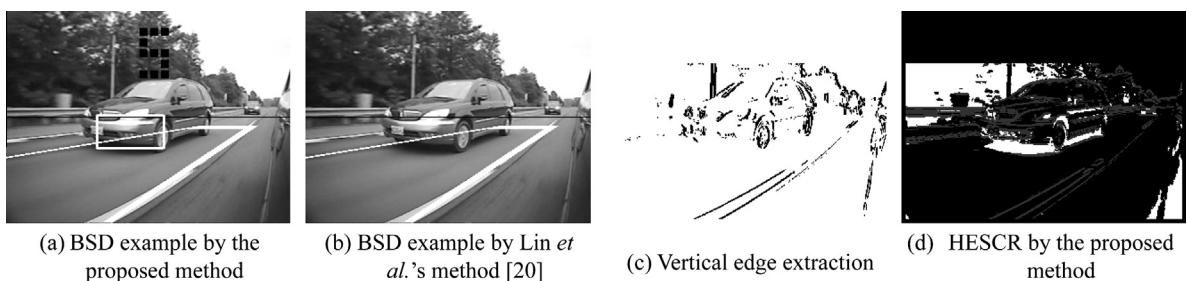| Lane	Detected vehicles	Falsely detected vehicles	Actual vehicles
Total no. vehicles in BSR	41	0	45
Detection score J of vehicles	91.11%		
Time span of the video	35 min		

under daytime conditions. It is observed that although there are loss detections, the proposed BSWS for daytime does not falsely detect vehicles because of the proposed method of non-vehicle obstacles elimination described in Section 4.4. The bright objects and non-vehicle obstacles will not be mis-detected.

Fig. 19 shows the detection results under nighttime conditions. Unlike daytime conditions, the detection under nighttime conditions is based on the paired headlights. As Fig. 19 shows, most of these vehicles in the blind spot region are accurately detected and tracked using the proposed system, though many non-vehicle illuminating objects, such as street lamps, reflected beams, and road reflectors on the ground appear extremely close to the lights of the detected vehicles.

Table 2 shows the experimental data of the proposed system of vehicle detection and tracking for the traffic scene shown in Fig. 19. Besides, the proposed BSWS does not falsely detect vehicles under the nighttime condition. This is because the proposed classification rules shown as Eqs. (26) and (27) can recognize the pairing headlights of vehicles precisely. Furthermore, by using the tracking process, the detected pairing headlights are certificated once more. Thus, the proposed BSWS prevents false detecting for nighttime. According to the results of the blind spot detection under daytime and nighttime conditions, the proposed system can provide favorable performances under both daytime and nighttime conditions.

The above experimental traffic video sequences in the daytime and nighttime were also employed for a comparative evaluation of vehicle detection performance. The following experiments evaluate the performance of the proposed system and compare with the Lin and Xu's vertical-edge based method [20] in the daytime and the Wang et al.'s paired-light-based method [16] at night. Fig. 20 presents the comparative results of the proposed system with the Lin and Xu's vertical-edge based method. Fig. 20a shows that the approaching vehicles are accurately detected using the proposed system, whereas in Fig. 20b, the Lin and Xu's vertical-edge based method cannot accurately detect the vehicles. This is because the vertical-edge feature of the target vehicle is shattered, as shown in Fig. 20c. Fig. 20d compares the proposed system, which adopts the HESCR, and the continuous level shadow detection, as described in Sections 4.2 and 4.3, respectively. The proposed system can efficiently retrieve the shadow region and determine the locations of the vehicles accurately. The comparative experimental data are also shown in Table 3.

Fig. 21 illustrates the comparisons of the proposed method with the Wang et al.'s paired-light-based method. As Fig. 21b shows, the reflections of the paired headlights were mis-detected using the Wang et al.'s method, because the area and the aspect ratio of the headlights are not considered comprehensively. Moreover, many occlusions and misdetections occur, as illustrated in Fig. 21d, because the lamp tracking mechanism is lacking. By contrast, the proposed system can resolve the occlusions and misdetections, and strengthens the detection results of target vehicles. The proposed system can detect

(a) BSD example by the proposed method   (b) BSD example by Lin *et al.*'s method [20]   (c) Vertical edge extraction   (d) HESCR by the proposed method

Fig. 20. Image pre-processing of the testing scene.

Table 3

Comparative experimental results of the proposed system and Lin et al.'s method.

Lane	Proposed method	Lin et al.'s method [20]
Detected warning vehicles	70	59
Falsely detected vehicles	0	0
Actual warning vehicles	72	
Detection score J of vehicles	97.22%	81.94%
Time span of the video	35 min	

(a) BSD Example 1 using the proposed method

(b) BSD Example 1 using Wang *et al.*'s method [16]

(c) BSD Example 2 by the proposed method

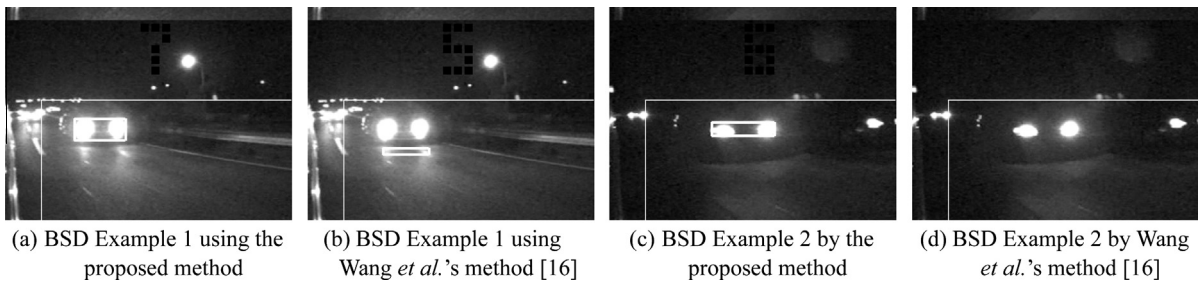(d) BSD Example 2 by Wang *et al.*'s method [16]

Fig. 21. Comparative results of BSD under nighttime conditions.

Table 4
Comparative experimental results of the proposed system and Wang et al.'s method.

Lane	Proposed method	Wang et al.'s method [16]
Detected warning vehicles	41	26
Falsely detected vehicles	0	4
Actual warning vehicles	45	
Detection score J of vehicles	91.11%	53.06%
Time span of the video	35 min	

the vehicle with paired headlights, as shown in Fig. 21a and c. The quantitative experimental data are shown in Table 4. As can be seen from the results shown in Tables 3 and 4, the proposed BSD system performs effectively in blind spot vehicle detection under both daytime and nighttime conditions.

6. Conclusions

An effective BSWS for daytime and nighttime conditions has been proposed in this paper. The proposed BSWS is fully vision-based and uses only two cameras that were installed below the rear view mirror on both sides of our camera-assisted experimental car, the Taiwan *i*TS-II. Before presenting the BSWS, a dynamic camera models are introduced using perspective transformation. To perform the BSD in daytime effectively, this study proposes the ROI for daytime based on the models of lane markings by using the presented camera models. After obtaining the ROI in daytime, the shadow edge features of the vehicle object are extracted using minimum ground plane pre-processing, HESCR, and continuous level shadow detection techniques. Moreover, this study presents the elimination approach of non-vehicle obstacles to improve the detection accuracy in daytime. Besides, this study employed bright object segmentation under nighttime conditions. The extracted bright objects were analyzed to determine whether they are lamp objects. Sequentially, the potential vehicle lamp objects are then verified to determine whether two of the lamp objects can be paired. Thus, when the paired headlights are found, the vehicles in the nighttime are detected. Additionally, the vehicle distance estimation is also implemented to forewarn the driver if any vehicle is approaching the host car. The proposed BSWS is implemented on a TI DM642 DSP-based embedded platform, operating at 600 MHz with 32 MB DRAM, and achieves an average of 20 and 50 frames per second to operate under both daytime and nighttime conditions. To evaluate vehicle detection performance quantitatively, the experimental video sequences having totaling more than 30 min captured in daytime and nighttime road scenes are adopted. The proposed system achieves high accuracy in vehicle detection performance, and the detection accuracy achieves up to 97.22% and 91.11% for daytime and nighttime conditions, respectively. Besides, this study implemented the existing researches and conducted the performance comparisons to the proposed BSWS in both daytime and nighttime conditions. The experimental results demonstrate that the proposed BSWS can provide robustness, high computational efficiency, and high vehicle detection accuracy for driver assistance and collision warning applications.

Acknowledgements

References

[1] Xie M. Trinocular vision for AGVguidance: path location and obstacle detection. Comput Electr Eng 1995;21(6):441–52.
[2] Ivetic D, Mihic S, Markoski B. Augmented AVI video file for road surveing. Comput Electr Eng 2010;36(1):169–79.
[3] Yu W, Xie S. An ant colony optimization algorithm for image edge detection. In: IEEE congr evol comput; 2008. p. 751–6.
[4] Fan SS. An improved CANNY edge detection algorithm. In: World congr software eng; 2009. p. 497–500.

[5] Yang W, Wang X, Moran B, Wheaton A, Cooley N. Efficient registration of optical and infrared images via modified Sobel edging for plant canopy temperature estimation. Comput Electr Eng 2012;38(5):1213–21.
[6] Vizireanu DN. Generalizations of binary morphological shape decomposition. J Electron Imaging 2007;16(1):01302. 1–6.
[7] Udrea RM, Vizireanu DN. Iterative generalization of morphological skeleton. J Electron Imaging 2007;16(1):010501. 1–3.
[8] Vizireanu DN, Halunga S, Marghescu G. Morphological skeleton decomposition interframe interpolation method. J Electron Imaging 2010;19(2):023018. 1–3.
[9] Vizireanu DN, Udrea RM. Visual-oriented morphological foreground content grayscale frames interpolation method. J Electron Imaging 2009;18(2):020502. 1–3.
[10] Vizireanu DN. Morphological shape decomposition interframe interpolation method. J Electron Imaging 2008;17(1):013007. 1–5.
[11] Salamy H. Minimizing address arithmetic instructions in embedded applications on DSPs. Comput Electr Eng 2012;38(6):1550–63.
[12] Furukawa K, Okada R, Taniguchi Y, Onoguchi K. Onboard surveillance system for automobiles using image processing LSI. In: Proc IEEE intell veh symp; 2004. p. 555–9.
[13] Chen CT, Chen YS. Real-time approaching vehicle detection in blind-spot area. In: Proc IEEE int'l conf intell transp syst; 2009. p. 1–6.
[14] Rodríguez Flórez SA, Frémont V, Bonnifait P, Cherfaoui V. Multi-modal object detection and localization for high integrity driving assistance. Mach Vision Appl 2011. http://dx.doi.org/10.1007/s00138-011-0386-0.
[15] Jia X, Hu Z, Guan H, A new multi-sensor platform for adaptive driving assistance system (ADAS). In: Proc world congr intell control autom; 2011. p. 1224–30.
[16] Wang CC, Huang SS, Fu LC. Driver assistance system for lane detection and vehicle recognition with night vision. In: Proc of IEEE/RSJ int'l conf intell rob syst; 2005. p. 3530–5.
[17] Fossati A, Schönmann P, Fua P. Real-time vehicle tracking for driving assistance. Mach Vision Appl 2011;22(2):439–48.
[18] O'Malley R, Jones E, Glavin M. Rear-lamp vehicle detection and tracking in low-exposure color video for night conditions. IEEE Trans Intell Transp Syst 2010;11(2):453–62.
[19] Hakawa H, Shibata T. Block-matching-based motion field generation utilizing directional edge displacement. Comput Electr Eng 2010;36(4):617–25.
[20] Lin M, Xu X. Multiple vehicle visual tracking from a moving vehicle. In: Proc the 6th int'l conf intell syst des appl; 2006. p. 373–8.
[21] Wong CY, Qidwai U. Intelligent surround sensing using fuzzy inference system. In: Proc IEEE int'l conf sens; 2005. p. 1034–7.
[22] Ruder M, Enkelmann W, Garnitz R. Highway lane change assistant. In: Proc IEEE int'l veh symp, vol. 1; 2002. p. 240–4.
[23] Otto C, Gerber W, León FP, Wirnitzer J. A joint integrated probabilistic data association filter for pedestrian tracking across blind regions using monocular camera and radar. In: Proc IEEE int'l veh symp; 2012. p. 636–41.
[24] Achler O, Trivedi MM. Vehicle wheel detector using 2D filter banks. In: Proc IEEE int'l veh symp; 2004. p. 25–30.
[25] Techmer A. Real-time motion analysis for monitoring the rear and lateral road. In: Proc IEEE int'l veh symp; 2004. p. 704–9.
[26] Díaz J, Ros E, Rotter SA, Muhlenberg M. Lane-change decision aid system based on motion-driven vehicle tracking. IEEE Trans Veh Technol 2008;57(5):2736–46.
[27] Krips M, Velten J, Kummert A, Teuner A. AdTM tracking for blind spot collision avoidance. In: Proc IEEE int'l veh symp; 2004. p. 544–8.
[28] Lin B-F, Chan Y-M, Fu L-C, Hsiao P-Y, Chuang L-A, Huang S-S, et al. Integrating appearance and edge features for sedan vehicle detection in the blind-spot area. IEEE Trans Intell Transp Syst 2012;13(2):737–47.
[29] Li S, Hai Y. Easy calibration of a blind-spot-free fisheye camera system using a scene of a parking space. IEEE Trans Intell Transp Syst 2011;12(1):232–42.
[30] Jeong S, Ban SW, Lee M. Autonomous detector using saliency map model and modified mean-shift tracking for a blind spot monitor in a car. In: Proc of IEEE int'l conf on mach learn appl; 2008. p. 253–8.
[31] Intelligent transport systems – lane change decision aid systems (LCDAS) – performance requirements and test procedures. Tech rep, ISO/FDIS 17387; 2008.
[32] Wu B-F, Lin C-T, Chen Y-L. Dynamic calibration and occlusion handling algorithms for lane tracking. IEEE Trans Ind Electron 2009;56(5):1757–73.
[33] Okada R, Taniguchi Y, Furukawa K, Onoguchi K. Obstacle detection using projective invariant and vanishing lines. In: Proc IEEE comput vision, vol. 1; 2003. p. 330–7.
[34] Chen Y-L, Wu B-F, Huang H-Y, Fan C-J. A real-time vision system for nighttime vehicle detection and traffic surveillance. IEEE Trans Ind Electron 2011;58(5):2030–44.
[35] Sneath P, Sokal R. Numerical taxonomy. The principle and practice of numerical classification. New York: W.H. Freeman; 1973.

Bing-Fei Wu received the Ph.D. degree in electrical engineering from the University of Southern California, Los Angeles, in 1992 and serves as the Director of the Institute of Electrical and Control Engineering, National Chiao Tung University in Taiwan. He is a Fellow of IEEE and the Chair of the Technical Committee on Intelligent Transportation Systems of IEEE Systems, Man and Cybernetics Society.

Hao-Yu Huang was born in Kaoshiung, Taiwan, R.O.C., in 1983. He received the B.S. and Ph.D. degree in electrical and control engineering from National Chiao Tung University, Hsinchu, Taiwan, in 2004 and 2012, respectively. His research interests include audio and video coding, image processing and embedded system design.

Chao-Jung Chen received his B.S. and M.S. degree in the Institute of Mechanical Engineering from Huafan University, Taiwan, in 1999 and 2001, respectively, and the Ph.D. degree in electrical and control engineering from the National Chiao-Tung University, Hsinchu, in 2006. He is currently the CEO of CSSP Inc., Hsinchu, Taiwan. His research interest is real-time image processing in intelligent transportation systems.

Ying-Han Chen was born in Tainan, Taiwan in 1981. He received the B.S. and M.S. degrees in electrical engineering from National Central University, Jhongli, Taiwan, in 2003 and 2006, respectively. He is currently working toward the Ph.D. degree in electrical engineering at National Chiao Tung University, Hsinchu, Taiwan. His research interests include computer networks, embedded systems, and digital signal processing.

Chia-Wei Chang received the B.S. degree in electrical engineering from National Central University, Jhongli, in 2003, and M.S. degree in electrical and control engineering from the National Chiao-Tung University, Hsinchu, in 2006. He is currently working at ZyXEL Communications Corporation. His research interests include image processing and computer vision.

Yen-Lin Chen received the B.S. and Ph.D. degree in electrical and control engineering from National Chiao Tung University, Hsinchu, Taiwan, in 2000 and 2006, respectively. He is an Associate Professor in the same institute at the Dept. of Computer Science and Information Engineering, National Taipei University of Technology, Taipei, Taiwan. His research interests include image and video processing, embedded systems, pattern recognition, intelligent vehicles, and intelligent transportation system.